Acta Oceanol. Sin., 2019, Vol. 38, No. 5, P. 1–9
https://doi.org/10.1007/s13131-019-1437-z
http://www.hyxb.org.cn
E-mail: hyxbe@263.net

A numerical simulation of the generation and evolution of nonlinear internal waves across the Kara Strait

Qun Li[1]*, Huiding Wu[1], Hongwei Yang[2], Zhanhai Zhang[1]

[1] Polar Research Institute of China, Ministry of Natural Resources, Shanghai 200136, China

[2] College of Mathematics and Systems Science, Shandong University of Science and Technology, Qingdao 266590, China

Received 2 November 2017; accepted 14 March 2018

Abstract

Nonlinear internal waves (NIWs) are ubiquitous around the Kara Sea, a part of the Arctic Ocean that is north of Siberia. Three hot spot sources for internal waves, one of which is the Kara Strait, have been identified based on Envisat ASAR. The generation and evolution of the NIWs through the interactions of the tide and topography across the strait is studied based on a nonhydrostatic numerical model. The model captures most wave characteristics shown by satellite data. A typical inter-packets distance on the Barents Sea side is about 25 km in summer, with a phase speed about 0.65 m/s. A northward background current may intensify the accumulation of energy during generation, but it has little influence on the other properties of the generated waves. The single internal solitary wave (ISW) structure is a special phenomenon that follows major wave trains, with a distance about 5–8 km. This wave is generated with the leading wave packets during the same tidal period. When a steady current toward the Kara Sea is included, the basic generation process is similar, but the waves toward the Kara Sea weaken and display an internal bore-like structure with smaller amplitude than in the control experiment. In winter, due to the growth of sea ice, stratification across the Kara Strait is mainly determined by the salinity, with an almost uniform temperature close to freezing. A pycnocline deepens near the middle of the water depth (Barents Sea side), and the NIWs process is not as important as the NIWs process in summer. There is no fission process during the simulation.

Key words: nonlinear internal wave, nonhydrostatic numerical model, Kara Sea, synthetic aperture radar

Citation: Li Qun, Wu Huiding, Yang Hongwei, Zhang Zhanhai. 2019. A numerical simulation of the generation and evolution of nonlinear internal waves across the Kara Strait. Acta Oceanologica Sinica, 38(5): 1–9, doi: 10.1007/s13131-019-1437-z

1 Introduction

The life cycle of nonlinear internal waves (NIWs) continues to be an active research area (Lee and Beardsley, 1974; da Silva et al., 2015; Zhao et al., 2016; Xu et al., 2016). A common generation mechanism involves stratified tidal flows over large-amplitude topography, such as sills, continental shelf-slope regions (Vlasenko et al., 2014), and submarine ridges (Buijsman et al., 2010; Wang et al., 2010; Xu et al., 2014).

Research focusing on the dynamics of the NIWs at high latitudes is sparse compared with studies at lower latitudes. Tides appear to be the main energy source supporting enhanced vertical mixing in the marginal seas of the Arctic Ocean and these may generate vertical heat fluxes greater than 50 W/m^2 (Rippeth et al., 2015). Internal gravity waves generated by tide-topography interactions and their ultimate breakup are a major mechanism for enhanced vertical mixing and dissipation rate over rough topography. The NIWs are ubiquitous around the Kara Sea, a sea on the margin of the Arctic Ocean (Kozlov et al., 2015; Morozov et al., 2008). Three hot spot sources for the internal waves, one of which is the Kara Strait, have been identified based on Envisat ASAR. The Kara Strait (with its center approximately 70.5°N, 58°E) is about 4° below the critical latitude of the semidiurnal internal tide. It is in northeastern Europe, between the Barents Sea and Kara Sea. Many field experiments have been conducted around the Kara Strait. Morozov et al. (2003) reported mooring records deployed inside the strait. Temperature fluctuations indicated an internal tide with M_2 frequency. Further observations were made about 10 a later (Morozov et al., 2008), using towed CTD measurements across the section from the Kara Sea to the Barents Sea. This section provided a snapshot of the vertical displacement of temperature, and indicated an internal bore structure toward the Barents Sea and a hydraulic jump just downstream (from south to north) of the sill. A radar image analysis shows short-period internal wave (IW) trains following the internal bore. Morozov et al. (2008) presented a 2-D nonhydrostatic numerical model for the observed phenomenon and this was consistent with the experimental results. However, they did not provide an analysis of the generation and evolution of the internal tide.

A linear theory predicts that the internal tide activity is suppressed close to or above the critical latitude, which is 74.5°E for M_2 frequency (Vlasenko et al., 2003). Vlasenko et al. (2003) noted that when nonlinearity of the generated waves was sufficiently strong, topography-scale short IWs were produced with characteristics similar to those of unsteady lee waves. Kurkina and Talipova (2011) modeled the generation and evolution process of

Foundation item: The National Key Research and Development Program of China under contract No. 2016YFC1402705; the National Natural Science Foundation of China under contract No. 41576189.
*Corresponding author, E-mail: liqun@pric.org.cn

large amplitude NIWs around Spitsbergen Island. They suggested that the strong nonlinear unsteady lee internal waves were generated by the barotropic tide in the Barents Sea above the critical latitude.

We studied the dynamic process of the NIWs across the Kara Strait using a 2-D nonhydrostatic numerical model. In this report, Section 2 presents observational evidence and background conditions. Numerical model configuration details are given in Section 3, and the model results are discussed in Section 4. A summary and discussion are presented in Section 5.

2 Background

2.1 *Observational evidence*

Severe weather and ice conditions limit the *in situ* observation of internal wave processes around the Kara Sea. Mooring and hydrographic section investigation across the Kara Strait in the summer of 1997 provided the first evidence of large-amplitude internal waves (≈10–20 m at 80 m water depth, with an upper layer approximately 25–30 m), and identified tide-sill interaction as the main mechanism.

In contrast to the *in situ* measurements, remote sensing is often used to capture the NIWs in the ocean, especially SAR imagery. Kozlov et al. (2015) made IW observations from July to October 2007 around the Kara Sea using satellite ENVISAT ASAR data. They presented spatial statistics of IW signatures and their properties in the Kara Sea. Three hot spot sources, one of which is the Kara Strait, were identified. Basic wave characteristics were consistent with previous *in situ* data. A group of typical ASAR images is shown in Fig. 1. At the initial time, the waves generated on both sides are nearly symmetric, with 2-D characteristics (Fig. 1a, BA wave towards the Barents Sea and KA wave toward the Kara Sea). After exiting the source region, the wave showed different characteristics that resembled wave trains on the Barents Sea side (Figs 1b and c, BA wave in two adjacent tidal periods) and the 3-D features were pronounced. A typical feature in Fig. 1b is two adjacent single-wave structures near the source region, separated by a distance of approximately 6 km (BA and BC waves). These features were verified in the modeling results.

2.2 *Bathymetry and stratification across the Kara Strait*

Bathymetry across the Kara Strait is asymmetric, with a depth of approximately 80 m in the Barents Sea and a depth of approximately 200 m in the Kara Sea (Fig. 2a). The length scale of the sill is approximately 20 km, with the shallowest depth of approximately 50 m (Fig. 2b). The slope is steeper on the Barents Sea side

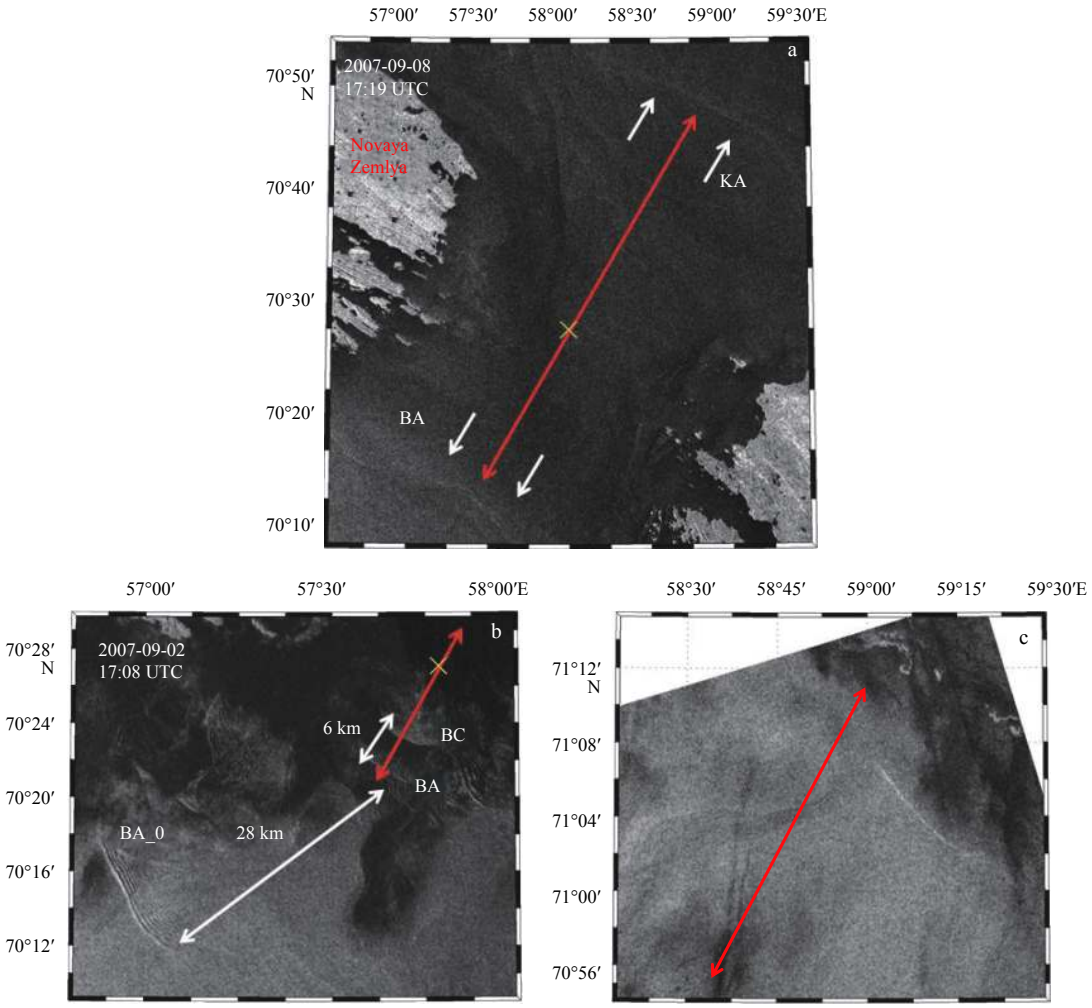

Fig. 1. ENVISAT ASAR images of internal waves (bore/packets) around the Kara Strait. The red line indicates topography section used in the model. The white line with double arrow indicates inter-packets distance. The white line with single arrow indicates particular wave. The "×" indicates the summit of the sill and the name of the wave is consistent with the name in the model results.

than on the Kara Sea side. The difference of the topography features between the sides may result in different properties of tide-induced IWs towards the opposite direction.

Stratification around the Kara Strait shows seasonal differences (Fig. 3). In summer, the upper layer has low salinity owing to the melting of sea ice, and its temperature increases through solar radiation absorption (Fig. 3a). This produces a strong gradient of temperature, salinity and density at the approximately 30 m depth (Fig. 3b, solid line). Below the pycnocline, stratification is weak. In winter, the sea ice cover may reach this region, producing a mixed layer of approximately 20 m of nearly freezing water and the salinity reaching approximately 32.5 (Fig. 3a, dashed line). Stratification in winter is mainly determined by the salinity because the temperature difference over the entire depth is small and the pycnocline is greater than 40 m (Fig. 3b, solid line).

2.3 *Tide and background current*

A tide analysis shows that the major axis of the tidal current is consistent with the cross-section of the strait, and the amplitude of the tide was approximately 0.2 m/s. There was a background current with amplitude of approximately 0.12 m/s from the Barents to the Kara Seas. Recent *in situ* measurements have verified the existence of tide-induced, large-amplitude IWs (Morozov et al., 2008).

Internal tides may be generated under the conditions of efficient tidal forcing and dramatically varying bathymetry combined with suitable stratification. Combining the bathymetry and stratification allows the calculation of a forcing term to quantify internal tide generation. This is

$$F(z) = 2\pi N^2(z)\, UH_x/(H\omega_f), \quad (1)$$

where U is the barotropic tidal current; H is water depth and ω_f is the forcing frequency (Pichon et al., 2013). Vertical integration $\int_0^H F(z)\,\mathrm{d}z$ of the forcing term provides evidence of a dominant region of the internal tide generation across the strait (Fig. 2b). The integrated forcing displays several IT excitation regions. The strongest of these occurs around the shallowest sill, and the second is downstream at a distance of approximately 10 km. These multiple structures increase the pattern complexity of generated IWs. Furthermore, forcing in summer was more than three

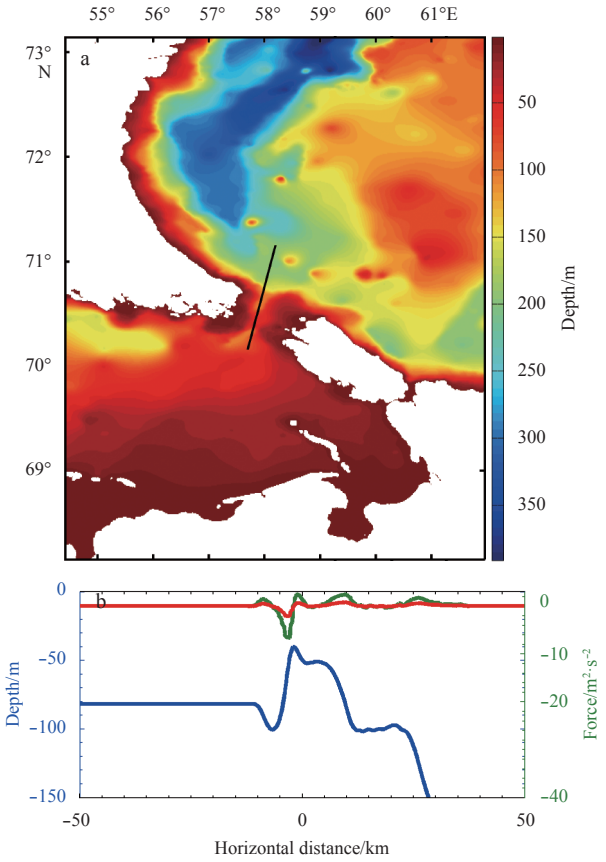

Fig. 2. Topography around Kara Strait and 2-D bathymetry section across the strait (black line) used in the model (bathymetry data from GEBCO1 min, (IOC, IHO, and BODC, 2003)) (a) and the vertical integrated forcing calculated with Eq. (1) (b). The green is summer stratification and the red is winter stratification.

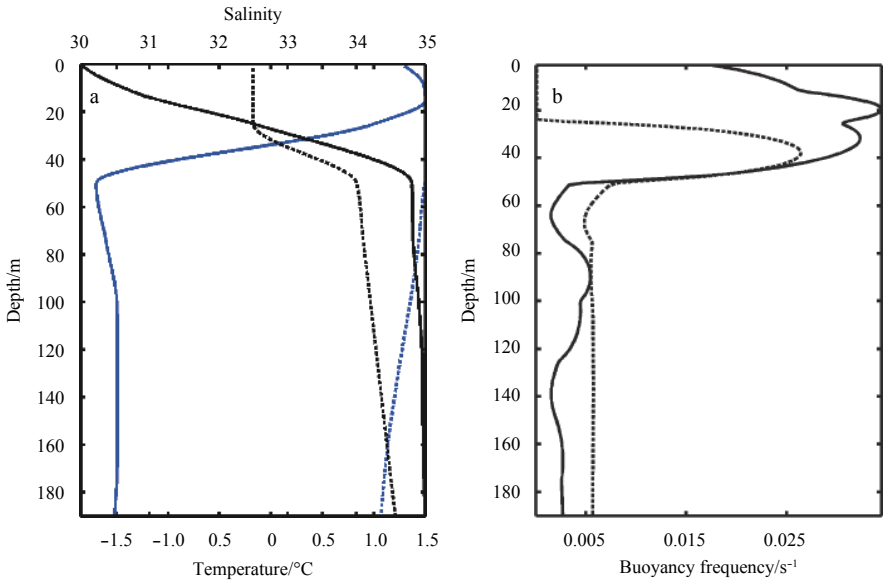

Fig. 3. Temperature (blue) and salinity (black) profiles from observations (Harms and Karcher, 1999) in summer (solid) and winter (dashed) (a) and corresponding buoyancy frequencies (solid black represents summer and dashed black winter) (b).

times greater than that in winter, because of the weaker and thinner pycnocline during winter (Fig. 2b).

3 Model configuration

The background conditions support the existence of tide-induced IWs, as verified by the *in situ* observations and ASAR data. Another effective method to investigate the dynamic processes is based on numerical modeling. We used the Massachusetts Institute of Technology general circulation model (MITgcm) for all of the numerical experiments (Marshall et al., 1997). The MITgcm integrates the incompressible Boussinesq equations, assuming a linear equation of state:

$$\frac{\partial}{\partial t}\vec{u}+\vec{u}\cdot\nabla\vec{u}+f\vec{k}\times\vec{u}=-\nabla p+b\vec{k}+\nu_{\mathrm{h}}\left(\frac{\partial^2}{\partial x^2}+\frac{\partial^2}{\partial y^2}\right)\vec{u}+\nu_{\mathrm{v}}\frac{\partial^2}{\partial z^2}\vec{u}, \tag{2}$$

$$\nabla\cdot\vec{u}=0, \tag{3}$$

$$\frac{\partial}{\partial t}b+\vec{u}\cdot\nabla b=k\nabla^2 b, \tag{4}$$

where $\vec{u}=(u,v,w)$ is the velocity vector; p is density-scaled pressure; t, x, y and z are time and space coordinates; b is buoyancy; ν_{h} and ν_{v} are horizontal and vertical viscosity constants; k is tracer diffusivity; f is the Coriolis parameter; and $\vec{k}$ is the unit vector in the vertical direction (see http://mitgcm.org, for more details).

In contrast with common large-scale processes in the ocean, the ISWs represent a balance of nonlinearity and dispersion, with the latter derived from a nonhydrostatic pressure. Therefore, we turned on the nonhydrostatic capability of the MITgcm in all of the experiments, allowing an explicit simulation of the dynamic properties of ISWs. A sufficiently high grid resolution was used to resolve mixing processes due to instability, and no sophisticated subgrid-scale mixing scheme was used. As in Vlasenko et al. (2014), the Richardson number-dependent parameterization for turbulent closure of the vertical viscosity ν and the diffusivity k (Pacanowski and Philander, 1981) was used:

$$\begin{aligned}\nu&=\frac{\nu_0}{(1+\alpha Ri)^n}+\nu_{\mathrm{b}},\\ k&=\frac{\nu}{(1+\alpha Ri)}+k_{\mathrm{b}},\end{aligned} \tag{5}$$

where $Ri=N^2(z)/\left(u_z^2+v_z^2\right)$ is the Richardson number; u and v are the components of horizontal velocity; ν_{b}=10^{-5} m^2/s and k_{b}=10^{-5} m^2/s are the background viscosity and diffusivity, respectively; ν_0=1.5×10^{-2} m^2/s; α=5 and n=1 are adjustable parameters. Such a parameterization increases ν and k in areas where Ri is small. The horizontal viscosity and diffusivity were set to a constant 0.5 m^2/s.

The horizontal computation domain had a length of 300 km and was comprised of 6 000 grid cells, with the sill summit at the center. The horizontal grid resolution around the focusing region was $\Delta x=20$ m, which is adequate to resolve most relevant processes in the model. These included the disintegration of the internal tides or lee waves and the subsequent generation of internal solitary wave trains. This resolution was increased to several hundreds of meters toward the open boundary. The choice of a horizontal grid is consistent with the resolution requirement in nonhydrostatic IW modeling (Vitousek and Fringer, 2011). There were 200 layers in the vertical dimension, with the deepest region of approximately 190 m on the Kara Sea side. The vertical grid resolution was $\Delta z=0.95$ m, and the time step $\Delta t=5$ s was used to keep the model stable.

The tide and the background current were applied on the open boundaries to keep the barotropic flow in phase on the south and north sides. By doing so, depth-integrated horizontal flow (volume flux) was independent of the horizontal coordinate (da Silva et al., 2015).

4 Results

4.1 *Results of linear theory*

With linear approximation and variable separation technologies, an eigenequation for the vertical mode structure (Cushman-Roisin and Beckers, 2011) can be derived:

$$\frac{\mathrm{d}^2}{\mathrm{d}z^2}\boldsymbol{W}+k_{\mathrm{h}}^2\frac{N^2(z)-\omega^2}{\omega^2-f^2}\boldsymbol{W}=0, \tag{6}$$

with boundary conditions $\boldsymbol{W}$= 0 at z = 0 and z = –H, corresponding to a rigid lid at the top and flat bottom. As an eigenvalue problem, there is an entire series of special (ω, k_{h}) values for which $\boldsymbol{W}(z)$ may be nonzero. These are called eigenvalues, and corresponding $\boldsymbol{W}(z)$ solutions are called eigenfunctions or, more specifically in this configuration, vertical modes. The normalized $\boldsymbol{W}(z)$ has a vertical structure of a different mode with (ω, k_{h}). The pair of (ω, k_{h}) represents the dispersion relation of the stratified ocean, from which we can examine basic wave properties under different stratifications. With the frequency of the M_2 tide, the first two modes with stratification used here were calculated and are presented in Fig. 4 for waves on the Barents Sea side. The maximum amplitude of the Mode 1 wave was around the pycnocline, while Mode 2 with two extremes was on both sides of the

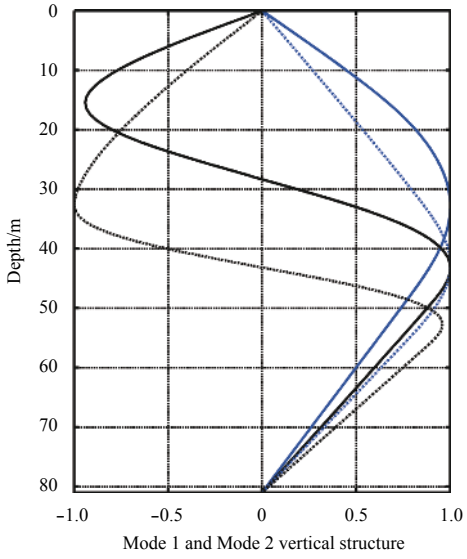

Fig. 4. Mode 1 and Mode 2 vertical structure function (from iwave, a Matlab program for the calculation of Eq. (4.1) (Cushman-Roisin and Beckers, 2011)) on the Barents Sea side (the solid blue line is Mode 1 with summer stratification and the solid black line is Mode 2 with summer stratification; the dashed blue is Mode 1 with winter stratification and the dashed black is Mode 2 with winter stratification).

pycnocline. In the winter case, the Mode 1 structure was almost symmetric, which may induce weak nonlinearity according to a KdV theory (Grimshaw et al., 2010).

We let $k_h \in [2\pi/(50\ \text{km}), 2\pi/(5\ \text{km})]$ be within the range of typical observation, and a series of corresponding frequency ω was calculated. Figure 5 shows this relation under the winter (dashed blue) and summer (solid blue) stratifications on the Barents Sea (at 81 m depth) side, along with the M_2 tide frequency (dashed red), $f = 1.37\times10^{-4}\text{s}^{-1}$ was used in the calculation (corresponding to latitude 70.5°N). The frequency and the wavelength have an inverse relation, i.e., lower-frequency waves are typically longer. At the frequency of the semidiurnal tides, we found the typical wavelength in the winter case to be 15 km, and in the summer case it was 23 km.

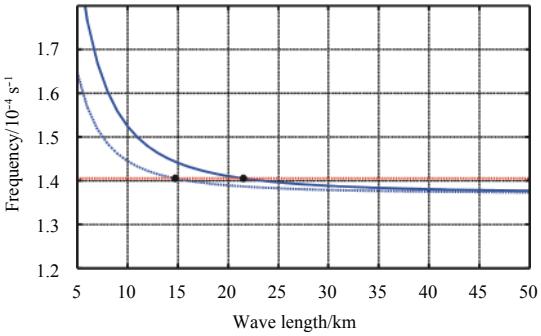

Fig. 5. Dispersion relation based on summer (solid blue curve) and winter (dot-dash blue line) stratification on Barents Sea (depth 81 m) side. The dot-dash red line shows M_2 tide frequency.

The basic parameter classifying the generation mechanism is the Froude number (Vlasenko et al., 2005), which is defined as the ratio of forcing current to phase speed of the generated baroclinic waves. Table 1 shows linear phase velocity results calculated using the mode equation, and they are used as a reference in the following analysis.

Table 1. Linear phase speed (m/s) for first two modes for two different local water depths, with summer and winter stratifications

	Speed			
	Summer		Winter	
	80 m	45 m	80 m	45 m
Mode 1	0.67	0.45	0.45	0.23
Mode 2	0.28	0.21	0.14	0.10

Note: Eighty meters was water depth on the Barents Sea side and 45 m was water depth at the sill crest.

4.2 *Model results*

Using the theoretical analysis, we investigated the details of the dynamic process of IW generation and evolution. We conducted three experiments, among which the reference experiment included only tide forcing (Table 2) and used the summer T/S profile shown in Fig. 3a. We also studied the sensitivity of model results via the other two experiments. One experiment had an additional steady current tuned to simulate the observed background current across the strait (northward) as forcing, and the other with the winter stratification.

4.2.1 *Generation and evolution of NIWs in reference experiments*

Figure 6 presents a Hovmöller diagram of displaced isopycnal at a depth of 25 m. A Phase speed is estimated from the

Table 2. Experiments configuration

Exp. ID	Forcing	Stratification	Forcing amplitude/m·s^{-1}
1	only semi-diurnal tide	summer	0.2 (U_{ti})
2	tides plus northward steady current	summer	0.2 (U_{ti}) + 0.12 (U_0)
3	only semi-diurnal tide	winter	0.2 (U_{ti})

Note: U_{ti} is the tide speed.

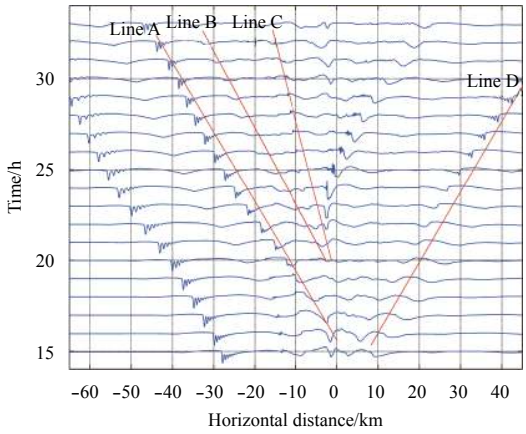

Fig. 6. Hovmöller diagram presenting displaced isopycnal at 25 m depth along the model transect, with time increasing vertically upward (1 h step). The red line A to C indicates the evolution of various wave trains generated during the same tidal period. Line D shows one ISWs toward the Kara Sea.

slope of Line A, Line B is approximately 0.69 m/s, and Line C is approximately 0.30 m/s, which is similar to the estimation based on the linear theory (Table 1). The spatial structure of the modeled mode-1 IW compared well with that captured by the ASAR image (Fig. 1) and *in situ* observations. The inter-ISW distance of O (0.5–1 km) after two tidal periods with leading wave amplitude approximately 15 m were similar to previous reports (Kozlov et al., 2015; Morozov et al., 2008). The distance between two main consecutive ISW packets was approximately 25 km on the Barents side, and a slightly larger distance on the Kara Sea side, from which we estimated a phase speed of approximately 0.72 m/s. This is consistent with the linear theory and estimation based on the slope of a single wave train in the Hovmöller diagram. Within one wave packet, nonlinear characteristics were clear when compared with the inter-ISW distance of the following two wave packets. For example, at t = 25 h in Fig. 6, inter-ISW distance increased from that at x = –27 km to the one at x = –55 km. If we follow the evolution of the isopycnal in Fig. 6 from t = 15 h, an isopycnal disturbance around the summit of the sill began splitting into two parts, one toward the Barents Sea and the other toward the Kara Sea. After about 6 h evolution (t = 21 h), nonlinear effects steepened the front of the initial disturbance and disintegration into a solitary structure began. Meanwhile, just behind this leading wave at a distance of approximately 5 km, a dome structure gradually split into two parts. One propagated along line B, with a phase speed similar to the leading wave train, and the other had a slower phase speed of approximately 0.30 m/s, which is consistent with the Mode 2 phase speed (Table 1). The wave indicated by Line B exhibited internal bore properties. Its speed was slower than the leading wave as seen in the first tidal period, when the distance of this structure from the leading wave front reached approximately 15 km. This process is clarified in

Fig. 7 because the evolution of one single isopycnal is insufficient to illustrate the multimodal structure.

The superposition of the baroclinic horizontal speed and isopycnal gives more detail on the IW generation process during tide-topography interaction. In Fig. 7, we present this superposition for one tidal period (t = 15–25 h). The horizontal baroclinic speed was calculated by the modeled horizontal speed minus the vertically integrated horizontal speed. This means that the integrated baroclinic horizontal speed was 0. Figure 7 shows this process from t = 15 h as in Fig. 6, i.e., the onset of generation of the southward disturbance during the second tidal period. From t = 15 h (F-1, Fig. 7a), the southward tidal current reached 0.46 m/s, which was close to its maximum. This was comparable with the phase speed of Mode 1 IWs at 45 m depth under the summer stratification (Table 1). Wave KA toward the Kara Sea released from the main sill, and with the increase of flooding current, a trough began to develop downstream of the main sill (Fig. 7b, t = 17 h). As the tidal current speed is still larger than the phase speed of Mode 1, the trough downstream of the sill became clearer (BA), and a Mode 2 convex type wave BB emerged just behind the BA wave. Its phase speed from the linear theory was approximately 0.3 m/s (Table 1), which means that it could be trapped for a longer time during the flooding. After about 1 h, the BA was released and propagated over the sill toward the Barents Sea. Subsequently, at t = 19 h, the trapped Mode 2 wave (BB) was finally released and passed over the summit of the sill (Fig. 7c). On the basis of snapshot of the vertical structure of the horizontal velocity field, this wave propagated toward the Barents Sea (Fig. 7c, BB wave).

From t = 21 h (Fig. 7d), nonlinear effects became increasingly important on both sides of the leading waves, which became steeper on their front side. Leading wave BA on the Barents Sea side even began to disintegrate. During this process, the Mode 2 type wave following the leading wave gradually decayed, becoming a blur away from the main topography. Wave BC emerged in Fig. 7e. After several hours of evolution (Fig. 7f), that wave evolved into an internal bore structure following the leading BA wave in the same tidal period, with a following distance of approximately 10 km.

A complete view of the baroclinic wave field after two tidal periods is shown in Fig. 8. Two clear ISW trains emerged, with an inter-packet distance of approximately 27 km, a result slightly larger than that from the linear theory. This is partially attributable to the nonlinear properties of the ISW trains. On the basis of the weakly nonlinear KdV theory (Grimshaw et al, 2010; Li and Farmer, 2011; Chen et al., 2014), the nonlinear contribution to the phase speed, $\alpha A/3$; $\alpha = 0.041\ 8$, is the nonlinear parameter on the Barents Sea side. With A=15 m, this contribution reached 20%–30%, which could explain the difference from the linear theory. On the Kara Sea side, the ISW trains were weaker than their

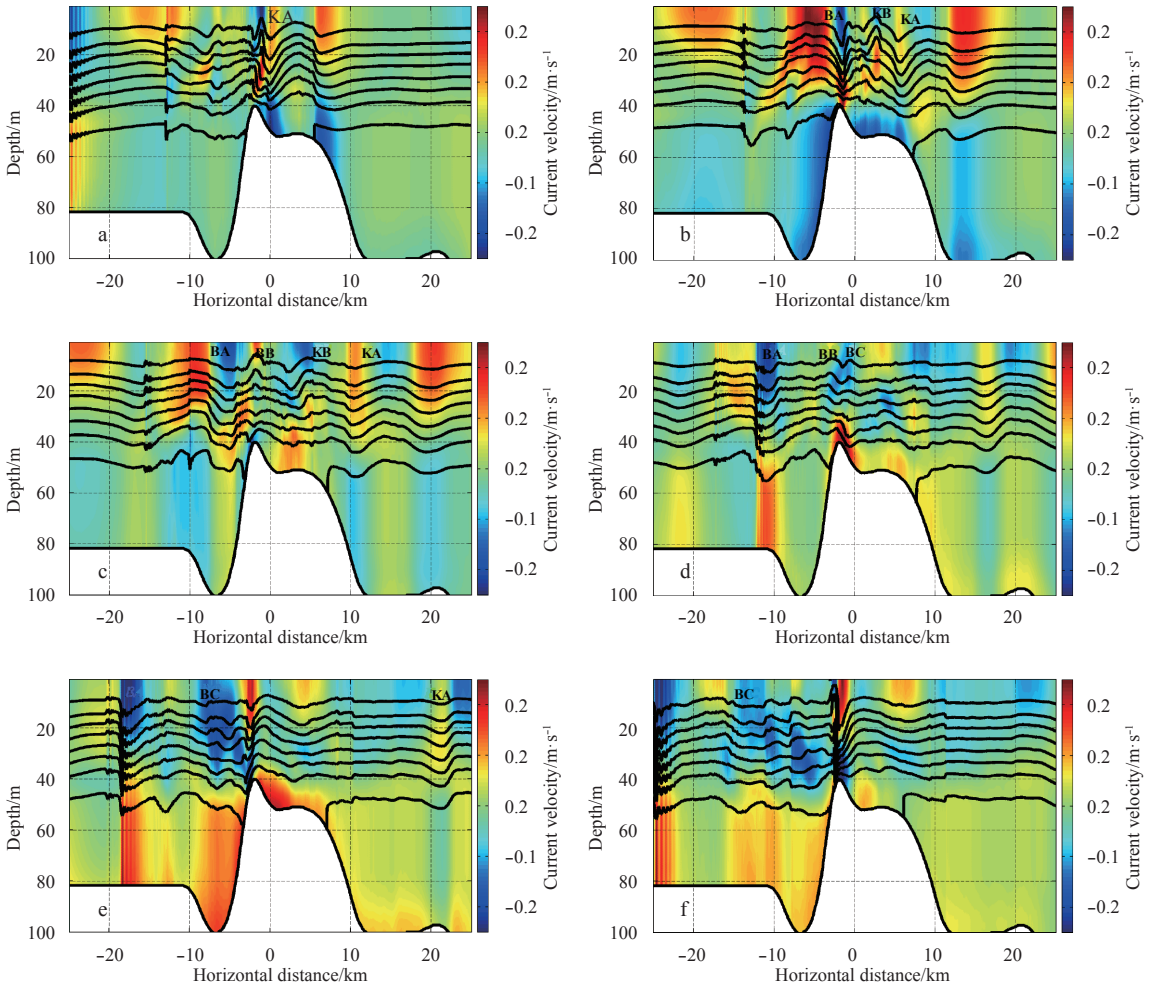

Fig. 7. Superposed baroclinic current together with isopycnal for t = 15–25 h. We defined that for flooding from the Barents to the Kara Sea, the start time was F-1 and every 2 h subsequently.

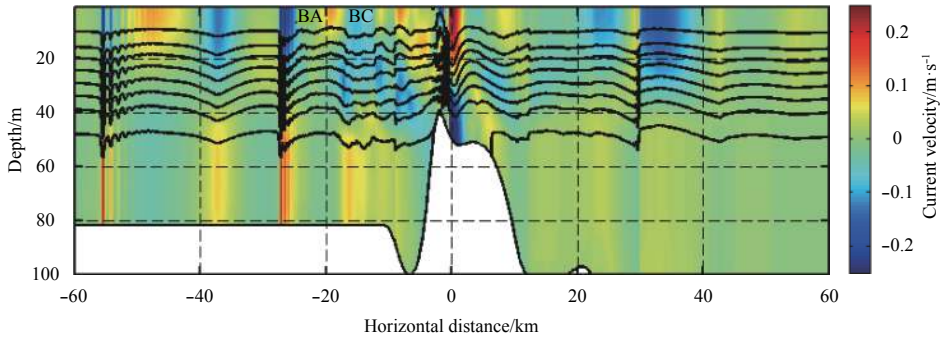

Fig. 8. Superposition of baroclinic current and isopycnal at t = 26 h.

counterparts on the Barents Sea, and a clear disintegration emerged at x = 30 km. The spatial characteristic of the wave from the previous period (x = −55 km), the leading wave train BA, and the following bore-like wave BC were similar to those captured in the ASAR image (Fig. 1c). The waves on both sides (BA and KA) had bore-like structures and little disintegration between −20 and 20 km, similar to those in Figs 1a and b.

4.2.2 *Influence of background current*

In the control experiment, only the tide was considered, and the final IW packets on the Barents Sea side were similar to typical observations. On the opposite side, the IW packets were weak but still clear. However, observations indicate that the wave toward the Kara Sea frequently has a single wave structure. Figure 9 shows a vertical section of the model results from the experiment with the background current (0.12 m/s) added. The generation process was similar to the reference experiment. The wave toward the Barents Sea was slowed by an opposing steady current and the amplitude of the generated wave was slightly stronger than the amplitude in the control experiment. The maximum Froude number in the tide-only experiment was close to 1, and together with the background, the Froude number was slightly larger than the critical value for the generation process of the wave on the Barents Sea side. This process may enhance the accumulation of initial energy and therefore increase the final wave packets. However, it decreases the energy of the waves toward the Kara Sea. Figure 9 shows that the disturbance on the Kara Sea side had a smaller vertical displacement and propagated with an internal bore structure (x = 43 km). No ISW trains emerged compared with the control experiment. Compared with the wave in the first tidal period at x = 68 km, the displacement was difficult to identify, meaning that dissipation of the internal bore structure was substantial compared with the solitary wave. The leading ISW in the first tidal period could drain energy from the initial disturbance to ultimately evolve into an isolated single wave. The amplitude of the wave train in the first tidal period was larger than that in the second tidal period, which had just begun the disintegration process.

4.2.3 *Influence of stratification*

The model results after two tidal periods in winter are presented in Fig. 10. The oscillations are more regular than the summer case. Owing to weak nonlinear characteristics of the winter stratification, there was no substantial disintegration, even though the wave amplitude was comparable to summer levels. Mode 1 phase speed in the winter case was 0.23 m/s at a depth of 45 m and 0.28 m/s at a depth of 55 m (Table 1). Thus, the energy accumulation time was longer during generation (longer trapped time). The phase speed of the Mode 2 wave was only 0.1 m/s, which means that it was nearly trapped around the topography during the entire tidal period, and the signal of the Mode 2 type wave was not as clear as in the summer case away from the topography. The wavelength of the internal tide (labeled in Fig. 10 between the vertical red lines) was approximately 16 km (Fig. 10), which is consistent with the linear theory. The trough around x = −22 km is similar to the internal bore structure in the summer case, and was generated in the same tidal period by a bulge of the topography at around x = 5 km. The lengths of the two troughs were consistent with the distance of the two sources. The difference is that the second wave in the winter case was stronger and comparable to the main wave (generated by the interaction of the tide and the sill centered around x = −4 km). This may have obscured the wave structure in a snapshot of the wave field (Fig. 10). Since the basic generation process is similar to that of the summer case, the full cycle is not shown here.

The effect of a steady current on the IT generation could be

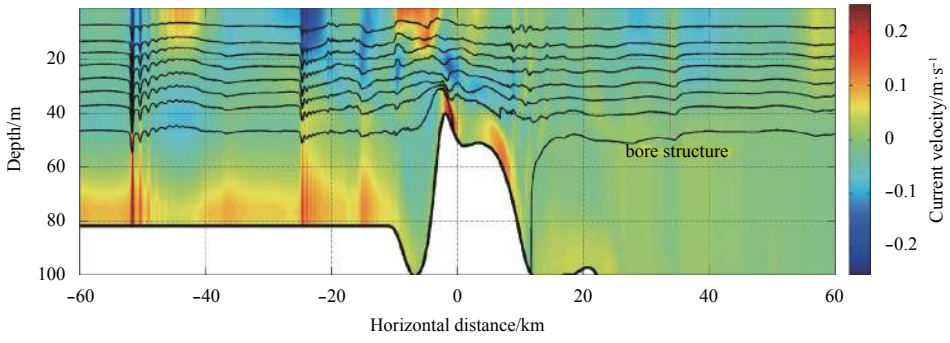

Fig. 9. Superposition of baroclinic current and isopycnal for t = 26 h with a background steady current.

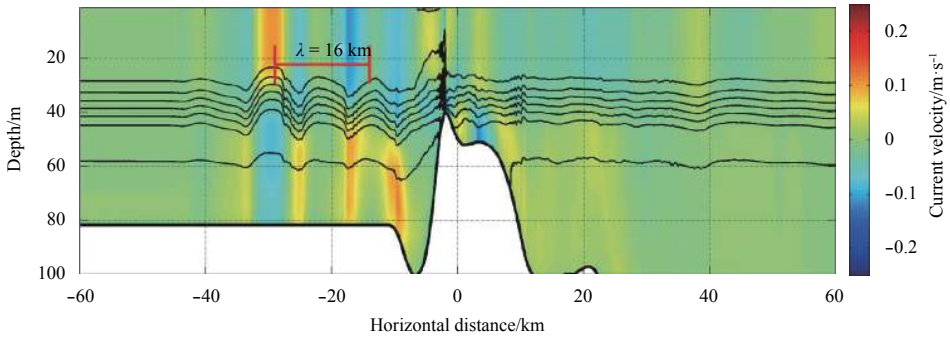

Fig. 10. Superposition of baroclinic current and isopycnal for t = 26 h under winter stratification.

explained by the Doppler effect (Li and Farmer, 2011), The Doppler shift induced by the superimposed flow changes the equivalent Froude number Fr_{Doppler}:

$$Fr_{\mathrm{Doppler}} = \frac{U_{ti}}{c \mp U_0}. \tag{7}$$

And so, the northward current increases the amplitude of internal tides propagating against the steady current (toward Barents Sea) but reduces the amplitude of the internal tide propagating with the current. Further analysis on the evolution of IT in Li and Farmer (2011) for the Luzon area employed a two-layer approximation. It revealed that the IT is expected to steepen because of nonlinearity, with rotation inhibiting but not preventing this. The parameters are the Ursell number U_r and nonhydrostatic dispersion, and the Ostrovsky number Q_s, which are ratios of nonlinearity to nonhydrostatic dispersion, and nonlinearity to rotation effect, respectively. For the two-layer system these are given by

$$U_r = \frac{AL^2\left(h_1 - h_2\right)}{h_1^2 h_2^2}, \tag{8}$$

$$Q_s = 12\pi^2\frac{\alpha A}{\gamma L^2} = \frac{36\pi^2 A g'\left(h_1 - h_2\right)}{f^2\lambda^2\left(h_1 + h_2\right)}, \tag{9}$$

where A and L are respectively the amplitude and length scale of the initial disturbance; h_1 and h_2 are the upper and lower layer depth; and g' is the reduced gravity. In the definition of Ostrovsky number, λ is wavelength of a simple harmonic wave. In the summer case, h_1 = 30 m and h_2 = 160 m, with typical amplitudes of 10 m for the initial disturbance and the length scale of the initial disturbance about 2–3 km (Fig. 6), the Ursell number is about 200, which means that nonhydrostatic effect plays a role at the initial time. Furthermore, the Ostrovsky number Q_s greater than 2 in the summer case, which means that the nonlinearity dominates and rotation plays a minor role. This process is clearly displayed in Fig. 6, where it can be seen that the disintegration process started just after the initial disturbance propagated over the sill. In the winter case, the Ostrovsky number is very small due to the small difference of a layer thickness, and thus the fission process is not important as in the summer case, as shown by the model results.

5 Summary

Remote sensing and *in situ* data revealed the widespread existence of the NIWs around the Kara Strait, which is an important channel for the northward transport of relatively warm Barents Sea water into the Arctic Ocean. Tidal properties, typical stratification in summer, and topography across the Kara Strait provide favorable conditions for the internal tide generation. The calculation of the phase speed based on the stratification shows that the flow is marginally critical. This claim is verified by the numerical simulations of the nonhydrostatic MITgcm, which was applied to a realistic 2-D bathymetry across the Kara Strait and driven by the barotropic tidal and the typical background current. In this study, a 2-D nonhydrostatic numerical simulation was employed to examine the generation and propagation properties of the ISWs. The model captured the basic wave characteristics shown by the satellite data. A typical wavelength on the Barents Sea side is about 25 km in summer, with a phase speed about 0.65 m/s. In the control experiment, the model successfully reproduced the single internal solitary wave (ISW) structure following the major wave trains, with a distance about 5–8 km (Fig. 1b), which was generated with the leading wave packets in the same tidal period. Meanwhile, the ISWs trains towards the Kara Sea were also obvious. When a steady current toward the Kara Sea is included, the basic generation process is similar, but the northward current increases the amplitude of the internal tides propagating against the steady current but reduces the amplitude of the internal tide propagating with the current, explained as Doppler effect during the internal tide generation (Li and Farmer, 2011). In this case, the waves toward the Kara Sea weakened and displayed an internal bore-like structure with smaller amplitude than in the control experiment, this was consistent with that in Figs 1a and c. With the winter stratification, the pycnocline weakened and deepens near the middle of the water depth (Barents Sea side), and thus the NIWs process is not as important as its counterpart in summer and there was no fission process during the simulation.

The ISWs are not restricted to the Kara Strait region. Two other hotspots are the southeastern part of the Novaya Zemlya Trough and the vicinity of Cape Zhelaniya (Kozlov et al., 2015). These may also be related to the tide and the typical topographic structure. Our calculations have captured the basic properties of the internal tide, but other characteristics have not been adequately explained. For example, after exiting from the main source region, 3-D characteristics weakened, and their evolution in most cases was no longer along the main axis of the cross-strait direction because of the topography and rotation effects. As a typical dynamic process in a stratified ocean, the generation and evolution of the NIWs at the study latitude were similar to other hotspots in the global ocean, but with a smaller wavelength because of proximity to the critical latitude. The Kara Strait plays a role in water exchange between the warm Barents Sea and cold

Kara Sea. Future work will focus on the role of the NIW in vertical mixing of the various water masses and its influence on the exchange processes across the Kara Strait.

Acknowledgments

We thank LetPub (www.letpub.com) for providing linguistic assistance during the preparation of this manuscript.

References

Buijsman M C, Kanarska Y, McWilliams J C. 2010. On the generation and evolution of nonlinear internal waves in the South China Sea. Journal of Geophysical Research, 115(C2): C02012, doi: 10.1029/2009JC005275

Chen Zhiwu, Xie Jieshuo, Wang Dongxiao, et al. 2014. Density stratification influences on generation of different modes internal solitary waves. Journal of Geophysical Research, 119(10): 7029–7046, doi: 10.1002/2014JC010069

Cushman-Roisin B, Beckers J M. 2011. Introduction to Geophysical Fluid Dynamics, Volume 101, Second Edition: Physical and Numerical Aspects. Englewood Clifts, NJ: Prentice Hall, 320

da Silva J C B, Buijsman M C, Magalhaes J M. 2015. Internal waves on the upstream side of a large sill of the Mascarene Ridge: a comprehensive view of their generation mechanisms and evolution. Deep-Sea Research: Part I. Oceanographic Research Papers, 99: 87–104, doi: 10.1016/j.dsr.2015.01.002

Grimshaw R, Pelinovsky E, Talipova T, et al. 2010. Internal solitary waves: propagation, deformation and disintegration. Nonlinear Processes in Geophysics, 17(6): 633–649, doi: 10.5194/npg-17-633-2010

Harms I H, Karcher M J. 1999. Modeling the seasonal variability of hydrography and circulation in the Kara Sea. Journal of Geophysical Research, 104(C6): 13431–13448, doi: 10.1029/1999JC900048

IOC, IHO and BODC. 2003. Centenary Edition of the GEBCO Digital Atlas, published on CD-ROM on behalf of the Intergovernmental Oceanographic Commission and the International Hydrographic Organization as part of the General Bathymetric Chart of the Oceans. Liverpool, UK: British Oceanographic Data Centre

Kozlov I E, Kudryavtsev V N, Zubkova E V, et al. 2015. Characteristics of short-period internal waves in the Kara Sea inferred from satellite SAR data. Izvestiya, Atmospheric and Oceanic Physics, 51(9): 1073–1087, doi: 10.1134/S0001433815090121

Kurkina O E, Talipova T G. 2011. Huge internal waves in the vicinity of the Spitsbergen Island (Barents Sea). Natural Hazards and Earth System Science, 11(3): 981–986, doi: 10.5194/nhess-11-981-2011

Lee C Y, Beardsley R C. 1974. The generation of long nonlinear internal waves in a weakly stratified shear flow. Journal of Geophysical Research, 79(3): 453–462, doi: 10.1029/JC079i003p00453

Li Qiang, Farmer D M. 2011. The generation and evolution of nonlinear internal waves in the deep basin of the South China Sea. Journal of Physical Oceanography, 41(7): 1345–1363, doi: 10.1175/2011JPO4587.1

Marshall J, Adcroft A, Hill C, et al. 1997. A finite-volume, incompressible Navier-Stokes model for studies of the ocean on parallel computers. Journal of Geophysical Research, 102(C3): 5753–5766, doi: 10.1029/96JC02775

Morozov E G, Paka V T, Bakhanov V V. 2008. Strong internal tides in the Kara Gates Strait. Geophysical Research Letters, 35(16): L16603, doi: 10.1029/2008GL033804

Morozov E G, Parrilla-Barrera G, Velarde M G, et al. 2003. The Straits of Gibraltar and Kara Gates: a comparison of internal tides. Oceanologica Acta, 26(3): 231–241, doi: 10.1016/S0399-1784(03)00023-9

Pacanowski R C, Philander S G H. 1981. Parameterization of vertical mixing in numerical models of tropical oceans. Journal of Physical Oceanography, 11(11): 1443–1451, doi: 10.1175/1520-0485(1981)011<1443:POVMIN>2.0.CO;2

Pichon A, Morel Y, Baraille R, et al. 2013. Internal tide interactions in the Bay of Biscay: observations and modelling. Journal of Marine Systems, 109–110: S26–S44, doi: 10.1016/j.jmarsys.2011.07.003

Rippeth T P, Lincoln B J, Yueng-Djern Lenn, et al. 2015. Tide-mediated warming of Arctic halocline by Atlantic heat fluxes over rough topography. Nature Geoscience, 8(3): 191–194, doi: 10.1038/NGEO2350

Vitousek S, Fringer O B. 2011. Physical vs. numerical dispersion in nonhydrostatic ocean modeling. Ocean Modelling, 40(1): 72–86, doi: 10.1016/j.ocemod.2011.07.002

Vlasenko V, Stashchuk N, Hutter K. 2005. Baroclinic Tides: Theoretical Modeling and Observational Evidence. Cambridge: Cambridge University Press, 372

Vlasenko V, Stashchuk N, Hutter K, et al. 2003. Nonlinear internal waves forced by tides near the critical latitude. Deep-Sea Research: Part I. Oceanographic Research Papers, 50(3): 317–338, doi: 10.1016/S0967-0637(03)00018-9

Vlasenko V, Stashchuk N, Inall M E, et al. 2014. Tidal energy conversion in a global hot spot: On the 3-D dynamics of baroclinic tides at the Celtic Sea shelf break. Journal of Geophysical Research, 119(6): 3249–3265, doi: 10.1002/2013JC009708

Wang Gang, Qiao Fangli, Dai Dejun. 2010. A 2D-numerical modeling of the generation and propagation of internal solitary waves in the Luzon Strait. Acta Oceanologica Sinica, 29(6): 1–11, doi: 10.1007/s13131-010-0071-6

Xu Zhenhua, Liu Kun, Yin Baoshu, et al. 2016. Long-range propagation and associated variability of internal tides in the South China Sea. Journal of Geophysical Research, 121(11): 8268–8286, doi: 10.1002/2016JC012105

Xu Zhenhua, Yin Baoshu, Hou Yijun, et al. 2014. Seasonal variability and north-south asymmetry of internal tides in the deep basin west of the Luzon Strait. Journal of Marine Systems, 134: 101–112, doi: 10.1016/j.jmarsys.2014.03.002

Zhao Zhongxiang, Alford M H, Girton J B, et al. 2016. Global observations of open-ocean mode-1 M_2 internal tides. Journal of Physical Oceanography, 46(6): 1657–1684, doi: 10.1175/JPO-D-15-0105.1